Progress In Electromagnetics Research C, Vol. 122, 95–108, 2022

Electromagnetic Wave Scattering Analysis by a Window Aperture on a Conducting Wall

Cuong M. Bui, Khanh N. Nguyen, and Hiroshi Shirai*

Abstract—High frequency electromagnetic plane wave scattering by a large rectangular glass window on a conducting wall has been analyzed in this study. Scattering far-fields are formulated by means of the Kirchhoff approximation in which the fields are obtained from radiation integrals due to the equivalent current sources on the virtually closed window apertures. In order to consider the effect of the window glass, a dielectric slab layer has been inserted in the window hole, and the reflection and transmission through the slab are treated via waveguide modal theory. The validity of our formulation has been confirmed by the numerical comparison with another method for an empty window case. The effects of the window dimension, the glass layer, and the polarization have been discussed for practical high frequency mobile communications.

1. INTRODUCTION

Recently, with the increasing popularity of using mobile devices, the outdoor-to-indoor wireless communication system is instrumental in providing fast and reliable communication channels between indoor subscribers and outdoor base stations through building walls and windows. In an urban area, high-frequency radio signals penetrate building walls, and the signals heavily attenuate due to the conduction loss of the wall material. Then, it may be natural to assume that the wall is conducting wall which yields no penetration, and window apertures would be primary gates for such communication. Therefore, a study of the scattering field of high-frequency electromagnetic waves by a window placed on the conducting wall plays a crucial role for understanding outdoor-indoor wireless communication pathway [1].

The evaluation of the scattering by a building window may be estimated from the scattering by a hole perforated on a thick conducting screen. Many works have been reported for estimating the electromagnetic scattering by slit/hole structures by utilizing various calculation methods [2–9], but these works have treated rather small apertures compared with the wavelength. Morse and Rubinstein analyzed the diffraction by a slit on an infinitely thin screen by an eigenfunction expansion in Mathieu functions [2]. Although this expansion solution exhibits rapid convergence for relatively narrow slits, the method is limited for the infinitely thin slit. For a thick conducting screen, Kashyap and Hamid [3] employed the Wiener-Hopf method and scattering matrix techniques. However, they mainly considered relatively narrow slit apertures. Also, the Fourier transform combined with the mode-matching technique has been successfully used to analyze high-frequency scattering by a narrow slit [4, 5]. This method may not be effective for high frequency scattering analysis because the method solves a time-consuming matrix equation which arises to assure the field continuity at the hole's aperture for determining the modal excitation coefficients. A hybrid method of finite element and boundary integral methods also gives efficient and accurate solutions for an inhomogeneously filled aperture [6],

Received 15 April 2022, Accepted 27 July 2022, Scheduled 5 August 2022
* Corresponding author: Hiroshi Shirai (shirai@elect.chuo-u.ac.jp).
The authors are with the Graduate School of Science and Engineering, Chuo University, Tokyo, Japan.

and a three-dimensional slot in a thick conducting plane [7]. Hongo and Ishii have applied the Weber-Schafheitlin integral to solve a diffraction by a thick conducting screen [8]. This method is called as Kobayashi Potential (KP) method, and has been extended to analyze a diffraction by a rectangular hole [9]. However, in a practical wireless communication scenario, when building windows dimensions are large compared with the wavelength, these methods may have numerical convergence problems, and require a large amount of memory and CPU time.

In the high-frequency regime, it would be better to apply asymptotic methods such as the Geometrical Theory of Diffraction (GTD) [10, 11] and Kirchhoff approximation (KA) [12–15]. While the GTD method gives pretty accurate results for estimating diffraction fields by canonical structures, the application to the present problem would be difficult, since one needs knowledge of diffraction coefficients by corners and dielectric wedges. Accordingly, the KA method is used in this study to formulate the scattering by a rectangular window aperture on a conducting wall.

The scattering by the window aperture can be treated as radiation from the equivalent magnetic current on the virtually closed aperture by the KA method. This study is an extension of the previous research on the scattering by a two-dimensional thick slit [14] and by rectangular empty hole [15]. Effect of window glass is now inserted to evaluate the more practical scattering effect of the building structure. This modification makes the formulation involved as it includes the reflection and transmission at the dielectric glass layer. Interactive contribution from the window hole is also considered as the secondary radiation field from the equivalent currents excited by the internal waveguide modal fields, in which the reflection and transmission at the glass layer can be treated rigorously.

This paper is structured as follows. The scattering far-field by a rectangular hole with a material slab layer is formulated in Section 2. Comparison with another method has been made to check the validity of our analysis, and some numerical results are presented in Section 3 to show the effect of the window aperture size, the glass layer, and the polarization, followed by the conclusion in Section 4. In the following discussion, the time-harmonic factor $e^{j\omega t}$ is assumed and suppressed throughout the context.

2. FORMULATION

Figure 1 describes an incident plane wave impinging on a rectangular hole of length a, width b, and thickness c on a thick conducting screen. Inside the hole, a window glass is simulated by a material slab layer whose relative material parameters are given by ε_r and μ_r, and the thickness is $c_2 - c_1$. For later analysis, the entire scattering region is divided into three regions: I) upper semi-infinite space ($z > 0$), II) inside the hole ($-c < z < 0$), III) lower semi-infinite space ($z < -c$).

An arbitrary polarized incident plane wave may be decomposed into two polarizations: the transverse electric (TE) and the transverse magnetic (TM) fields with respect to the incident plane and written as

$$\mathbf{E}^{\mathrm{i}} = (E^{\mathrm{TM}}\hat{\boldsymbol{\theta}}_0 + E^{\mathrm{TE}}\hat{\boldsymbol{\phi}}_0)e^{-j\mathbf{k}^{\mathrm{i}}\cdot\mathbf{r}}, \tag{1}$$

$$\mathbf{H}^{\mathrm{i}} = \sqrt{\frac{\varepsilon_0}{\mu_0}}(-E^{\mathrm{TM}}\hat{\boldsymbol{\phi}}_0 + E^{\mathrm{TE}}\hat{\boldsymbol{\theta}}_0)e^{-j\mathbf{k}^{\mathrm{i}}\cdot\mathbf{r}}, \tag{2}$$

where $\mathbf{k}^{\mathrm{i}}$ (with $|\mathbf{k}^{\mathrm{i}}| = k = \omega\sqrt{\varepsilon_0\mu_0}$), $\mathbf{r}$, ε_0 and μ_0 represent the free space incident wave number vector, the position vector to the observation point, the free space permittivity and permeability, respectively. Symbol '^' denotes the unit vector. In what follows, TE and TM polarizations will be analyzed separately.

By the Kirchhoff Approximation (KA) method [12–15], the scattering field may be given by the radiation from the magnetic currents on the closing aperture of the hole, as shown in Figure 2. The magnetic current sources $\mathbf{M}_1^{\pm}$ excite a scattering field $\mathbf{E}_1^{\mathrm{s}}$ in the upper region ($z > 0$) and a field $\mathbf{E}^{\mathrm{w}}$ inside the hole ($-c_2 < z < 0$). The field $\mathbf{E}^{\mathrm{w}}$ experiences the reflection and transmission at the slab layer and generates additional current sources $\mathbf{M}_{11}$ at the upper aperture and $\mathbf{M}_2$ at the lower aperture to yield the secondary scattering field to the exterior region I and III. The field inside the hole may be expressed in terms of rectangular waveguide modes, so that the reflection and transmission of the modal field at the material layer can be calculated theoretically by using waveguide modal theory. In region I, there also exists a reflected field due to the conducting screen at $z = 0$, and this contribution is omitted in the following analysis.

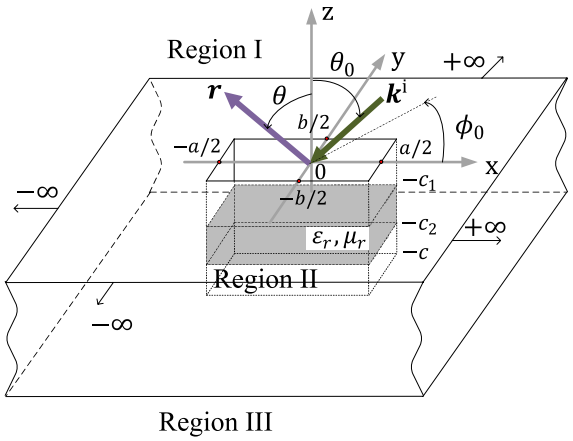

Figure 1. A rectangular hole in a thick conducting screen.

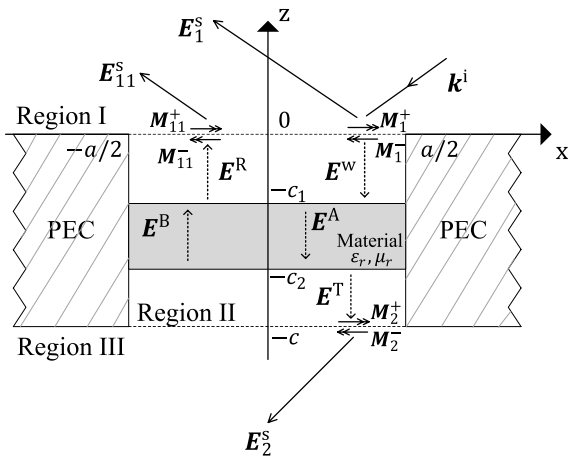

Figure 2. Cross sectional view and scattering process through the rectangular hole.

2.1. TE Polarization

Equivalent currents $\mathbf{M}_1^{\pm}$ on the virtually closed upper aperture ($|x| < a/2$, $|y| < b/2$, $z = 0_{\pm}$) may be derived from the incident electric field as [12]

$$\mathbf{M}_1^{\pm}(x, y, z = 0_{\pm}) = \mathbf{E}^{\mathrm{i}}|_{z=0_{\pm}} \times (\pm\hat{\mathbf{z}}) = \pm E^{\mathrm{TE}}(\cos\phi_0\hat{\mathbf{x}} + \sin\phi_0\hat{\mathbf{y}})e^{jk(x\sin\theta_0\cos\phi_0 + y\sin\theta_0\sin\phi_0)}. \quad (3)$$

The current $\mathbf{M}_1^{+}$ excites the primary scattering field $\mathbf{E}_1^{\mathrm{s}}$, while the current $\mathbf{M}_1^{-}$ excites the field $\mathbf{E}^{\mathrm{w}}$ inside the hole.

2.1.1. Primary Scattering Field $\mathbf{E}_1^{\mathrm{s}}$

In region I, the scattered field $\mathbf{E}_1^{\mathrm{s}}$ may be derived as a radiation from the above equivalent magnetic source $\mathbf{M}_1^{+}$ through a vector potential $\mathbf{F}_1$ as [16]

$$\mathbf{E}_1^{\mathrm{s}} = -\frac{1}{\varepsilon_0}\nabla \times \mathbf{F}_1. \quad (4)$$

When an observation point is located far from the hole, the vector potential $\mathbf{F}_1$ can be approximately calculated as

$$\mathbf{F}_1 \sim \frac{\varepsilon_0 e^{-jkr}}{2\pi r}\int_{S'} \mathbf{M}_1^{+}(\mathbf{r}')e^{jk\mathbf{r}'\cdot\hat{\mathbf{r}}}dS' = \frac{\varepsilon_0 e^{-jkr}}{2\pi r}\int_{S'} \mathbf{M}_1^{+}(\mathbf{r}')e^{jk(x'\sin\theta\cos\phi + y'\sin\theta\sin\phi)}dS', \quad (5)$$

where S' denotes the aperture ($|x'| < a/2$, $|y'| < b/2$, $z' = 0_{+}$) where the equivalent current $\mathbf{M}_1^{+}$ exists. $\mathbf{r}'$ is the position vector to the aperture source point on S' as

$$\mathbf{r}' = x'\hat{\mathbf{x}} + y'\hat{\mathbf{y}} + z'\hat{\mathbf{z}}. \quad (6)$$

After the vector potential $\mathbf{F}_1$ is evaluated analytically, the primary scattering far-field $\mathbf{E}_1^{\mathrm{s}}$ can be obtained from Eq. (4) by ignoring r^{-2} and higher order terms as

$$E_{1r}^{\mathrm{s}} \sim 0, \quad (7)$$

$$E_{1\theta}^{\mathrm{s}} \sim \frac{-2jE^{\mathrm{TE}}}{\pi kr}e^{-jkr}A\sin(\phi_0 - \phi), \quad (8)$$

$$E_{1\phi}^{\mathrm{s}} \sim \frac{2jE^{\mathrm{TE}}}{\pi kr}e^{-jkr}A\cos\theta\cos(\phi_0 - \phi), \quad (9)$$

where

$$A = \frac{\sin[(ka/2)(\sin\theta_0\cos\phi_0 + \sin\theta\cos\phi)]}{\sin\theta_0\cos\phi_0 + \sin\theta\cos\phi}\frac{\sin[(kb/2)(\sin\theta_0\sin\phi_0 + \sin\theta\sin\phi)]}{\sin\theta_0\sin\phi_0 + \sin\theta\sin\phi}. \quad (10)$$

2.1.2. Modal Field $\mathbf{E}^{\mathrm{w}}$ *inside the Hole*

While the upper equivalent current $\mathbf{M}_1^+$ yields the upper scattering field $\mathbf{E}_1^{\mathrm{s}}$, the lower equivalent current $\mathbf{M}_\mathbf{1}^-$ in Eq. (3) excites the field $\mathbf{E}^{\mathrm{w}}$ in the hole which is considered as a rectangular waveguide. Thus, the modal field propagating downward can be derived by Hertz potentials Π' and Π'' [17]:

$$\mathbf{E}^{\mathrm{w}}(\mathbf{r},\mathbf{r}') = \nabla\times\nabla\times\hat{\mathbf{z}}\Pi'(\mathbf{r},\mathbf{r}') - j\omega\mu_0\nabla\times\hat{\mathbf{z}}\Pi''(\mathbf{r},\mathbf{r}'), \tag{11}$$

$$\mathbf{H}^{\mathrm{w}}(\mathbf{r},\mathbf{r}') = j\omega\mu_0\nabla\times\hat{\mathbf{z}}\Pi'(\mathbf{r},\mathbf{r}') + \nabla\times\nabla\times\hat{\mathbf{z}}\Pi''(\mathbf{r},\mathbf{r}'), \tag{12}$$

where these potentials are expressed by other scalar potentials $\mathcal{S}'$, $\mathcal{S}''$ as [17]:

$$\Pi'(\mathbf{r},\mathbf{r}') = -\mathbf{M}_1^-(\mathbf{r}')\cdot\nabla'\times\hat{\mathbf{z}}S'(\mathbf{r},\mathbf{r}'), \tag{13}$$

$$\Pi''(\mathbf{r},\mathbf{r}') = -\frac{j}{\omega\mu}\mathbf{M}_1^-(\mathbf{r}')\cdot\nabla'\times\nabla'\times\hat{\mathbf{z}}S''(\mathbf{r},\mathbf{r}'), \tag{14}$$

with ∇, ∇' being operators applied for coordinates (x,y,z) and (x',y',z'), respectively. Potentials $\mathcal{S}'(\mathbf{r},\mathbf{r}')$ and $\mathcal{S}''(\mathbf{r},\mathbf{r}')$ can be derived by utilizing the Dirichlet and Neumann boundary conditions at the waveguide wall as [15, 17]:

$$\begin{aligned}\mathcal{S}'(\mathbf{r},\mathbf{r}') = &\sum_{m=1}^{\infty}\sum_{n=1}^{\infty}\frac{-2je^{-jk_{m,n}|z-z'|}}{abk_{m,n}[(m\pi/a)^2+(n\pi/b)^2]}\\ &\cdot\sin\Big[\frac{m\pi}{a}\Big(x+\frac{a}{2}\Big)\Big]\sin\Big[\frac{n\pi}{b}\Big(y+\frac{b}{2}\Big)\Big]\sin\Big[\frac{m\pi}{a}\Big(x'+\frac{a}{2}\Big)\Big]\sin\Big[\frac{n\pi}{b}\Big(y'+\frac{b}{2}\Big)\Big],\end{aligned} \tag{15}$$

$$\begin{aligned}\mathcal{S}''(\mathbf{r},\mathbf{r}') = &\sum_{m=0}^{\infty}\sum_{n=0}^{\infty}\frac{-j\epsilon_m\epsilon_n e^{-jk_{m,n}|z-z'|}}{2abk_{m,n}[(m\pi/a)^2+(n\pi/b)^2]}\\ &\cdot\cos\Big[\frac{m\pi}{a}\Big(x+\frac{a}{2}\Big)\Big]\cos\Big[\frac{n\pi}{b}\Big(y+\frac{b}{2}\Big)\Big]\cos\Big[\frac{m\pi}{a}\Big(x'+\frac{a}{2}\Big)\Big]\cos\Big[\frac{n\pi}{b}\Big(y'+\frac{b}{2}\Big)\Big],\end{aligned} \tag{16}$$

where $k_{m,n}$ is the modal wavenumber in z-direction

$$k_{m,n} = k\sqrt{1-(m\pi/ka)^2-(n\pi/kb)^2}, \tag{17}$$

and

$$\epsilon_i = \begin{cases}1 & (i=0)\\ 2 & (i>0).\end{cases} \tag{18}$$

Substituting $\mathbf{M}_1^-$ into Eqs. (13), (14), the field inside the hole may be obtained by integrating over the aperture source. Then the field is found to be TE_{mn} rectangular waveguide modes only. Thus, the components of waveguide fields can be derived directly from Eqs. (11), (12), or a representative H_z^{w} component as

$$H_z^{\mathrm{w}} = \sqrt{\frac{\varepsilon_0}{\mu_0}}\sum_{m=0}^{\infty}\sum_{n=0}^{\infty}F_{m,n}^{\mathrm{w}}e^{jk_{m,n}z}\cos\Big[\frac{m\pi}{a}\Big(x+\frac{a}{2}\Big)\Big]\cos\Big[\frac{n\pi}{b}\Big(y+\frac{b}{2}\Big)\Big], \tag{19}$$

where

$$F_{m,n}^{\mathrm{w}} = \frac{\pi^2\epsilon_m\epsilon_n E^{TE}}{k^2ab}B_{m,n}^0[(mkb)^2+(nka)^2]\sin\theta_0\cos\phi_0\sin\phi_0, \tag{20}$$

with $B_{m,n}^0$ is given as

$$\begin{aligned}B_{m,n}^0 = &\frac{(-1)^{m+1}e^{j(ka/2)\sin\theta_0\cos\phi_0}+e^{-j(ka/2)\sin\theta_0\cos\phi_0}}{(m\pi)^2-(ka\sin\theta_0\cos\phi_0)^2}\\ &\cdot\frac{(-1)^{n+1}e^{j(kb/2)\sin\theta_0\sin\phi_0}+e^{-j(kb/2)\sin\theta_0\sin\phi_0}}{(n\pi)^2-(kb\sin\theta_0\sin\phi_0)^2}.\end{aligned} \tag{21}$$

When the rectangular waveguide modal fields are incident on the material slab layer as in Figure 2, modal reflection and transmission occur. These reflected and transmitted modal fields from the slab

can be derived rigorously from the waveguide modal theory with the reflection coefficient $R_{m,n}$ and the transmission coefficient $T_{m,n}$ as

$$R_{m,n} = \frac{[(k'_{m,n})^2 - (\mu_r k_{m,n})^2](e^{j2k'_{m,n}(c_1-c_2)} - 1)e^{-j2k_{m,n}c_1}}{(k'_{m,n} + \mu_r k_{m,n})^2 - (k'_{m,n} - \mu_r k_{m,n})^2 e^{j2k'_{m,n}(c_1-c_2)}}, \tag{22}$$

$$T_{m,n} = \frac{4\mu_r k_{m,n} k'_{m,n} e^{j(k'_{m,n}-k_{m,n})(c_1-c_2)}}{(k'_{m,n} + \mu_r k_{m,n})^2 - (k'_{m,n} - \mu_r k_{m,n})^2 e^{j2k'_{m,n}(c_1-c_2)}}, \tag{23}$$

with $k'_{m,n}$ is the modal wavenumber in z-direction inside the slab layer as

$$k'_{m,n} = k\sqrt{\varepsilon_r\mu_r - (m\pi/ka)^2 - (n\pi/kb)^2}. \tag{24}$$

2.1.3. Secondary Scattering Field $\mathbf{E}^{\mathrm{s}}_{11}$

In the case of an empty hole ($\varepsilon_r = \mu_r = 1$ or $c_1 = c_2$), one can easily show that $R_{m,n} = 0$, $T_{m,n} = 1$, and the formulation coincides with the previous derived results in Ref. [15]. The reflected modal field $\mathbf{E}^{\mathrm{R}}$ propagates toward the upper aperture and radiates the secondary scattering field $\mathbf{E}^{\mathrm{s}}_{11}$ in region I. This scattering field can be calculated from the equivalent magnetic current $\mathbf{M}^{+}_{11}$ which is given as

$$\begin{aligned}
&\mathbf{M}^{\pm}_{11}(x, y, z = 0_{\pm}) = \mathbf{E}^{\mathrm{R}}|_{z=0_{\pm}} \times (\pm\hat{\mathbf{z}}) \\
&= \mp\sqrt{\frac{\varepsilon_0}{\mu_0}} \sum_{m=0}^{\infty}\sum_{n=0}^{\infty} \frac{j\omega\mu_0 R_{m,n} F^{\mathrm{w}}_{m,n}}{k^2 - k^2_{m,n}} \\
&\quad \cdot \left\{ \frac{m\pi}{a} \sin\left[\frac{m\pi}{a}\left(x + \frac{a}{2}\right)\right] \cos\left[\frac{n\pi}{b}\left(y + \frac{b}{2}\right)\right]\hat{\mathbf{x}} + \frac{n\pi}{b} \cos\left[\frac{m\pi}{a}\left(x + \frac{a}{2}\right)\right] \sin\left[\frac{n\pi}{b}\left(y + \frac{b}{2}\right)\right]\hat{\mathbf{y}} \right\}.
\end{aligned} \tag{25}$$

Then, the secondary scattering field $\mathbf{E}^{\mathrm{s}}_{11}$ induced by $\mathbf{M}^{+}_{11}$ at $z = 0_+$ can be derived by the same manner as $\mathbf{E}^{\mathrm{s}}_{1}$. One gets

$$E^{\mathrm{s}}_{11r} \sim 0, \tag{26}$$

$$E^{\mathrm{s}}_{11\theta} \sim \frac{j(k^2ab)^2 e^{-jkr}}{2\pi kr} \sum_{m=0}^{\infty}\sum_{n=0}^{\infty} \frac{R_{m,n} F^{\mathrm{w}}_{m,n} B_{m,n}}{(m\pi/ka)^2 + (n\pi/kb)^2} \left[\left(\frac{n\pi}{kb}\cos\phi\right)^2 - \left(\frac{m\pi}{ka}\sin\phi\right)^2\right] \sin\theta, \tag{27}$$

$$E^{\mathrm{s}}_{11\phi} \sim -\frac{j(k^2ab)^2 e^{-jkr}}{8\pi kr} \sum_{m=0}^{\infty}\sum_{n=0}^{\infty} \frac{R_{m,n} F^{\mathrm{w}}_{m,n} B_{m,n}}{(m\pi/ka)^2 + (n\pi/kb)^2} \left[\left(\frac{m\pi}{ka}\right)^2 + \left(\frac{n\pi}{kb}\right)^2\right] \sin(2\theta)\sin(2\phi), \tag{28}$$

where

$$\begin{aligned}
B_{m,n} = &\frac{(-1)^{m+1} e^{j(ka/2)\sin\theta\cos\phi} + e^{-j(ka/2)\sin\theta\cos\phi}}{(m\pi)^2 - (ka\sin\theta\cos\phi)^2} \\
&\cdot \frac{(-1)^{n+1} e^{j(kb/2)\sin\theta\sin\phi} + e^{-j(kb/2)\sin\theta\sin\phi}}{(n\pi)^2 - (kb\sin\theta\sin\phi)^2}.
\end{aligned} \tag{29}$$

It is noted that the equivalent magnetic current $\mathbf{M}^{-}_{11}$ at $z = 0_-$ excites the modal field which cancels the reflected modal field due to the virtually closed aperture. This matches with the physical nature of KA that there is no reflection at the aperture interface.

2.1.4. Lower Scattering Field $\mathbf{E}^{\mathrm{s}}_{2}$

The waveguide modal field $\mathbf{E}^{\mathrm{T}}$ creates equivalent currents $\mathbf{M}^{\pm}_{2}$ on the lower aperture of the hole ($z = -c$). The current $\mathbf{M}^{\pm}_{2}$ at $z = -c$ is determined by the following equation:

$$\begin{aligned}
\mathbf{M}^{\pm}_{2}(x, y, z = -c_{\pm}) &= \mathbf{E}^{\mathrm{T}}|_{z=-c_{\pm}} \times (\pm\hat{\mathbf{z}}) \\
&= \mp\sqrt{\frac{\varepsilon_0}{\mu_0}} \sum_{m=0}^{\infty}\sum_{n=0}^{\infty} \frac{j\omega\mu_0 T_{m,n} F^{\mathrm{w}}_{m,n} e^{-jk_{m,n}c}}{k^2 - k^2_{m,n}}
\end{aligned}$$

$$\cdot \left\{ \frac{m\pi}{a} \sin\left[\frac{m\pi}{a}\left(x+\frac{a}{2}\right)\right] \cos\left[\frac{n\pi}{b}\left(y+\frac{b}{2}\right)\right]\hat{\mathbf{x}} + \frac{n\pi}{b}\cos\left[\frac{m\pi}{a}\left(x+\frac{a}{2}\right)\right] \sin\left[\frac{n\pi}{b}\left(y+\frac{b}{2}\right)\right]\hat{\mathbf{y}} \right\}. \quad (30)$$

Again the current $\mathbf{M}_2^+$ excites the cancelling field of the reflected modal field to yield no modal reflection at the lower aperture. The current $\mathbf{M}_2^-$ excites the scattering far-field $\mathbf{E}_2^{\mathrm{s}}$ in the lower region ($z < -c$). By the same manner as in Section 2.1.1, the scattering far-field $\mathbf{E}_2^{\mathrm{s}}$ can be obtained as

$$E_{2r}^{\mathrm{s}} \sim 0, \quad (31)$$

$$E_{2\theta}^{\mathrm{s}} \sim -\frac{j(k^2ab)^2 e^{-jk(r+c\cos\theta)}}{2\pi kr} \sum_{m=0}^{\infty}\sum_{n=0}^{\infty} \frac{T_{m,n}F_{m,n}^{\mathrm{w}}B_{m,n}\sin\theta e^{-jk_{m,n}c}}{(m\pi/ka)^2+(n\pi/kb)^2} \left[\left(\frac{n\pi}{kb}\cos\phi\right)^2 - \left(\frac{m\pi}{ka}\sin\phi\right)^2\right], \quad (32)$$

$$E_{2\phi}^{\mathrm{s}} \sim \frac{j(k^2ab)^2 e^{-jk(r+c\cos\theta)}}{8\pi kr} \sum_{m=0}^{\infty}\sum_{n=0}^{\infty} T_{m,n}F_{m,n}^{\mathrm{w}}B_{m,n}e^{-jk_{m,n}c}\sin(2\theta)\sin(2\phi). \quad (33)$$

2.2. TM Polarization

The corresponding results for the TM polarization can be derived in a similar way as the TE polarization. Accordingly, the final results are shown without the detailed derivation.

2.2.1. Primary Scattering Field $\mathbf{E}_1^{\mathrm{s}}$

Based on KA, equivalent currents $\mathbf{M}_1^{\pm}$ on the virtually closed upper aperture may be derived for ($|x| < a/2$, $|y| < b/2$, $z = 0_{\pm}$) as

$$\begin{aligned}\mathbf{M}_1^{\pm}(x,y,z=0_{\pm}) &= E^{\mathrm{TM}} e^{-j\mathbf{k}^{\mathrm{i}}\cdot\mathbf{r}}\hat{\theta}_0\Big|_{z=0_{\pm}} \times (\pm\hat{\mathbf{z}}) \\ &= \pm E^{\mathrm{TM}}(\cos\theta_0\sin\phi_0\hat{\mathbf{x}} - \cos\theta_0\cos\phi_0\hat{\mathbf{y}}) e^{jk(x\sin\theta_0\cos\phi_0 + y\sin\theta_0\sin\phi_0)}. \end{aligned} \quad (34)$$

Then the scattering far-field $\mathbf{E}_1^{\mathrm{s}}$ may be derived from Eq. (4) with the vector potential $\mathbf{F}_1$ in Eq. (5) as

$$E_{1r}^{\mathrm{s}} \sim 0, \quad (35)$$

$$E_{1\theta}^{\mathrm{s}} \sim \frac{2jE^{\mathrm{TM}}\cos\theta_0}{\pi kr} e^{-jkr} A\cos(\phi_0-\phi), \quad (36)$$

$$E_{1\phi}^{\mathrm{s}} \sim \frac{2jE^{\mathrm{TM}}\cos\theta_0}{\pi kr} e^{-jkr} A\cos\theta\sin(\phi_0-\phi), \quad (37)$$

where A is given in Eq. (10)

2.2.2. Modal Field $\mathbf{E}^{\mathrm{w}}$ *inside the Hole*

While the field $\mathbf{E}^{\mathrm{w}}$ may be derived as in the previous Section 2.1.2, from the equivalent current $\mathbf{M}_1^-$, it is found that the internal modal field $\mathbf{E}^{\mathrm{w}}$ in the hole is expressed by both TM_{mn} and TE_{mn} rectangular waveguide modes. These waveguide modal fields can be derived from representative longitudinal components E_z^{w} and H_z^{w}:

$$E_z^{\mathrm{w}} = k\sum_{m=1}^{\infty}\sum_{n=1}^{\infty} \frac{\overline{G}_{m,n}^{\mathrm{w}}}{k_{m,n}} e^{jk_{m,n}z} \sin\left[\frac{m\pi}{a}\left(x+\frac{a}{2}\right)\right]\sin\left[\frac{n\pi}{b}\left(y+\frac{b}{2}\right)\right], \quad (38)$$

$$H_z^{\mathrm{w}} = \sqrt{\frac{\varepsilon_0}{\mu_0}}\sum_{m=0}^{\infty}\sum_{n=0}^{\infty} \overline{F}_{m,n}^{\mathrm{w}} e^{jk_{m,n}z} \cos\left[\frac{m\pi}{a}\left(x+\frac{a}{2}\right)\right]\cos\left[\frac{n\pi}{b}\left(y+\frac{b}{2}\right)\right], \quad (39)$$

where

$$\overline{G}_{m,n}^{\mathrm{w}} = -2mn\pi^2 E^{\mathrm{TM}} B_{m,n}^0 \sin(2\theta_0), \quad (40)$$

$$\overline{F}_{m,n}^{\mathrm{w}} = \frac{\pi^2\epsilon_m\epsilon_n E^{\mathrm{TM}}}{2k^2ab} B_{m,n}^0 [(mkb)^2\sin^2\phi_0 - (nka)^2\cos^2\phi_0]\sin(2\theta_0), \quad (41)$$

with $B^0_{m,n}$ is given in Eq. (21).

According to the waveguide modal theory, there is no modal coupling between TE and TM modes as these modal fields experience a slab layer discontinuity in the waveguide. Thus TE and TM modal fields can be treated separately. While the reflection coefficient $R_{m,n}$ and the transmission coefficient $T_{m,n}$ for TE_{mn} mode are given in Eqs. (22), (23), the corresponding $\overline{R}_{m,n}$ and $\overline{T}_{m,n}$ for TM_{mn} modes are found as

$$\overline{R}_{m,n} = \frac{[(k'_{m,n})^2 - (\varepsilon_r k_{m,n})^2](e^{j2k'_{m,n}(c_1-c_2)} - 1)e^{-j2k_{m,n}c_1}}{(k'_{m,n} + \varepsilon_r k_{m,n})^2 - (k'_{m,n} - \varepsilon_r k_{m,n})^2 e^{j2k'_{m,n}(c_1-c_2)}}, \tag{42}$$

$$\overline{T}_{m,n} = \frac{4\varepsilon_r k_{m,n} k'_{m,n} e^{j(k'_{m,n}-k_{m,n})(c_1-c_2)}}{(k'_{m,n} + \varepsilon_r k_{m,n})^2 - (k'_{m,n} - \varepsilon_r k_{m,n})^2 e^{j2k'_{m,n}(c_1-c_2)}}, \tag{43}$$

with $k_{m,n}$, $k'_{m,n}$ are given in Eqs. (17), (24), respectively.

2.2.3. Secondary Scattering Field $\mathbf{E}^{\mathrm{s}}_{11}$

The secondary scattering field $\mathbf{E}^{\mathrm{s}}_{11}$ due to the reflected modal field $\mathbf{E}^{\mathrm{R}}$ may be derived from the equivalent current $\mathbf{M}^{+}_{11}$ at the aperture. This current $\mathbf{M}^{+}_{11}$ is given as

$$\begin{aligned}
\mathbf{M}^{+}_{\mathbf{11}}(x,y,z=0_+) &= \mathbf{E}^{\mathrm{R}}|_{z=0_+} \times \hat{\mathbf{z}} \\
&= \sum_{m=0}^{\infty}\sum_{n=0}^{\infty} \frac{j}{(m\pi/ka)^2 + (n\pi/kb)^2} \\
&\quad \cdot \Big\{ -\Big(\frac{m\pi}{ka} R_{m,n}\overline{F}^{\mathrm{w}}_{m,n} + \frac{n\pi}{kb}\overline{R}_{m,n}\overline{G}^{\mathrm{w}}_{m,n}\Big) \sin\Big[\frac{m\pi}{a}\Big(x+\frac{a}{2}\Big)\Big] \cos\Big[\frac{n\pi}{b}\Big(y+\frac{b}{2}\Big)\Big]\hat{\mathbf{x}} \\
&\quad + \Big(\frac{n\pi}{kb} R_{m,n}\overline{F}^{\mathrm{w}}_{m,n} - \frac{m\pi}{ka}\overline{R}_{m,n}\overline{G}^{\mathrm{w}}_{m,n}\Big) \cos\Big[\frac{m\pi}{a}\Big(x+\frac{a}{2}\Big)\Big] \sin\Big[\frac{n\pi}{b}\Big(y+\frac{b}{2}\Big)\Big]\hat{\mathbf{y}}\Big\}.
\end{aligned} \tag{44}$$

Then, the secondary scattering far-field $\mathbf{E}^{\mathrm{s}}_{11}$ may be obtained from $\mathbf{M}^{+}_{\mathbf{11}}$ as

$$E^{\mathrm{s}}_{11r} \sim 0, \tag{45}$$

$$\begin{aligned}
E^{\mathrm{s}}_{11\theta} &\sim \frac{j(k^2ab)^2 e^{-jkr}}{2\pi kr} \sum_{m=0}^{\infty}\sum_{n=0}^{\infty} \frac{B_{m,n}\sin\theta}{(m\pi/ka)^2 + (n\pi/kb)^2} \\
&\quad \cdot \Big\{ R_{m,n}\overline{F}^{\mathrm{w}}_{m,n}\Big[\Big(\frac{n\pi}{kb}\cos\phi\Big)^2 - \Big(\frac{m\pi}{ka}\sin\phi\Big)^2\Big] - \frac{mn\pi^2}{k^2ab}\overline{R}_{m,n}\overline{G}^{\mathrm{w}}_{m,n}\Big\},
\end{aligned} \tag{46}$$

$$E^{\mathrm{s}}_{11\phi} \sim -\frac{j(k^2ab)^2 e^{-jkr}}{8\pi kr} \sum_{m=0}^{\infty}\sum_{n=0}^{\infty} R_{m,n}\overline{F}^{\mathrm{w}}_{m,n} B_{m,n} \sin(2\theta)\sin(2\phi), \tag{47}$$

where $B_{m,n}$ is given in Eq. (29).

2.2.4. Lower Scattering Field $\mathbf{E}^{\mathrm{s}}_{2}$

The scattering field $\mathbf{E}^{\mathrm{s}}_{2}$ in the lower half plane ($z < -c$) may be derived from the equivalent current $\mathbf{M}^{-}_{2}$ at the lower aperture ($z = -c$). The equivalent current $\mathbf{M}^{-}_{2}$ for calculating the radiation field in the lower half-space can be evaluated as

$$\begin{aligned}
\mathbf{M}^{-}_{2}(x,y,z=-c_-) &= \mathbf{E}^{\mathrm{T}}|_{z=-c_-} \times (-\hat{\mathbf{z}}) \\
&= \sum_{m=0}^{\infty}\sum_{n=0}^{\infty} \frac{je^{-jk_{m,n}c}}{(m\pi/ka)^2 + (n\pi/kb)^2} \\
&\quad \cdot \Big\{ \Big(\frac{m\pi}{ka} T_{m,n}\overline{F}^{\mathrm{w}}_{m,n} - \frac{n\pi}{kb}\overline{T}_{m,n}\overline{G}^{\mathrm{w}}_{m,n}\Big) \sin\Big[\frac{m\pi}{a}\Big(x+\frac{a}{2}\Big)\Big] \cos\Big[\frac{n\pi}{b}\Big(y+\frac{b}{2}\Big)\Big]\hat{\mathbf{x}} \\
&\quad + \Big(\frac{n\pi}{kb} T_{m,n}\overline{F}^{\mathrm{w}}_{m,n} + \frac{m\pi}{ka}\overline{T}_{m,n}\overline{G}^{\mathrm{w}}_{m,n}\Big) \cos\Big[\frac{m\pi}{a}\Big(x+\frac{a}{2}\Big)\Big] \sin\Big[\frac{n\pi}{b}\Big(y+\frac{b}{2}\Big)\Big]\hat{\mathbf{y}}\Big\}.
\end{aligned} \tag{48}$$

The scattering far-field $\mathbf{E}_2^{\mathrm{s}}$ can be derived from the above current $\mathbf{M}_2^-$ as

$$E_{2r}^{\mathrm{s}} \sim 0, \tag{49}$$

$$E_{2\theta}^{\mathrm{s}} \sim -\frac{j(k^2ab)^2 e^{-jk(r+c\cos\theta)}}{2\pi kr} \sum_{m=0}^{\infty}\sum_{n=0}^{\infty} \frac{e^{-jk_{m,n}c}}{(m\pi/ka)^2+(n\pi/kb)^2} B_{m,n}\sin\theta \cdot \left\{ T_{m,n}\overline{F}_{m,n}^{\mathrm{w}} \left[\left(\frac{n\pi}{kb}\cos\phi\right)^2 - \left(\frac{m\pi}{ka}\sin\phi\right)^2 \right] + \frac{mn\pi^2}{k^2ab}\overline{T}_{m,n}\overline{G}_{m,n}^{\mathrm{w}} \right\}, \tag{50}$$

$$E_{2\phi}^{\mathrm{s}} \sim \frac{j(k^2ab)^2 e^{-jk(r+c\cos\theta)}}{8\pi kr} \sum_{m=0}^{\infty}\sum_{n=0}^{\infty} T_{m,n}\overline{F}_{m,n}^{\mathrm{w}} e^{-jk_{m,n}c} B_{m,n}\sin(2\theta)\sin(2\phi). \tag{51}$$

3. NUMERICAL RESULTS AND DISCUSSION

The newly derived formulas in the previous section are now utilized for the evaluation of the scattering effect through the hole which can be considered as a rectangular window on a building wall. All numerical computation results are obtained by self-built Fortran code. In the following numerical calculation, all scattering far-field patterns are normalized by a common factor $e^{-jkr}/(2\pi kr)$ with $E^{\mathrm{TE}} = E^{\mathrm{TM}} = 1$.

The scattering far-fields are represented as a summation of radiations from magnetic currents due to an original incident plane wave and the TE and TM waveguide modes from the hole. The double formal infinite summations of modal reradiation fields can be easily truncated by those with the propagating modes only, since the effect from higher order evanescent modes decays rapidly. This truncation can be determined when the waveguide modal propagation constant $k_{m,n}$ in Eq. (17) becomes from a real to a complex number, as the modal indices m, n become large [14]. In our calculation, the first few evanescent waveguide modes are included for the numerical evaluation in order to make sure the numerical convergence.

Let us first discuss the empty hole case. As mentioned before, our formula is found to be analytically the same as the previous formulation for the empty case [15] when one removes the slab layer by setting $c_1 = c_2$ or $\varepsilon_r = \mu_r = 1$. In a previous study [15], we have shown that the scattering patterns can be easily estimated from the corresponding cross-sectional patterns of two-dimensional thick slit results if the incident plane is parallel to the hole's internal wall ($\phi_0 = 0, \pi/2, \ldots$). Accordingly, the incident angles are chosen here for general cases. Figure 3 shows the field distribution of the co-polarized component E_ϕ when the TE polarized plane wave is incident on a large rectangular empty hole ($ka = kb = 30$, $kc = 2$, $\theta_0 = \pi/6$, $\phi_0 = \pi/4$). While Figure 3(a) shows the three-dimensional scattering patterns, Figures 3(b), (c) are field strength maps projected on the spherical surfaces from the upper and the lower hemispheres. As one expects, the main scattering beams point to the specular reflection and transmission directions

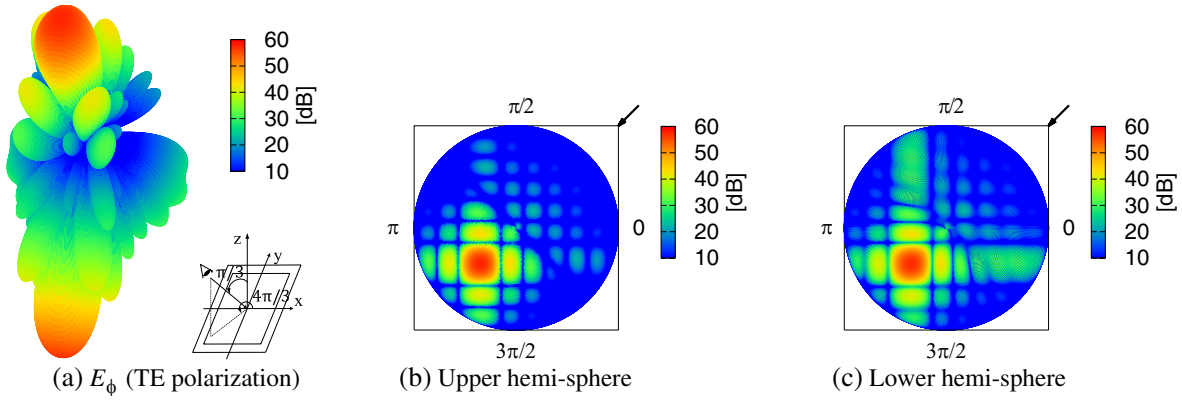

(a) E_ϕ (TE polarization) (b) Upper hemi-sphere (c) Lower hemi-sphere

Figure 3. TE scattering far-field patterns of E_ϕ component by an empty square window. $\theta_0 = \pi/6$, $\phi_0 = \pi/4$, $ka = kb = 30$, $kc = 2$. (a) Three-dimensional pattern viewing from $\theta = \pi/3$, $\phi = 4\pi/3$. (b) Scattering field strength map on the upper hemisphere. (c) Scattering field strength map on the lower hemisphere.

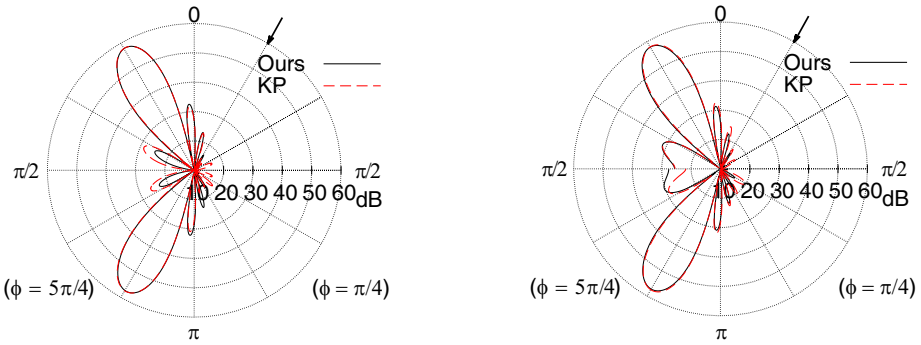

(a) TE polarization (b) TM polarization

Figure 4. Comparison of the scattering far-field patterns in θ variation in the incident plane ($\phi = \phi_0, \pi + \phi_0$), $\theta_0 = \pi/6$, $\phi_0 = \pi/4$, $ka = kb = 30$, $kc = 2$. (a) E_ϕ (TE polarization), (b) E_θ (TM polarization).

in the incident plane. One may note little effect of the thickness of the wall to region III, since the thickness of the wall is chosen as rather thin ($kc = 2$) with respect to the wavelength. Figure 4 shows the scattering field pattern of $E_\phi(E_\theta)$ in the incident plane for TE(TM) polarization. Our results are compared with those by the KP method [9]. While our result for the main lobe matches well with the KP method, one finds some differences at some side lobes near the boundaries. These differences stem from the fact that our approximation does not satisfy the boundary conditions on the virtually closed surfaces for the tangential fields and it ignores multiple edge diffraction terms [18]. One also observes that the main difference between the TE and TM polarizations arises in the strength of the side-lobes, and these lobes in the incident plane for the TM polarization are bigger than those for the TE polarization. In Figure 4 and the subsequent polar plots, there is a thick screen (wall) between the upper and lower semicircles. Accordingly, it is natural to have some discontinuities from top to bottom values, except for an infinitely thin screen case, and the fields show correct behavior along the wall surfaces.

The thickness effect of the hole to the scattering field distribution may be obtained for a rather deep case $kc = \sqrt{6}ka$ in Figure 5. While our modal excitation coefficients are given by KA, the waveguide modes themselves satisfy correctly the boundary conditions on the guided walls and the propagation mechanism inside the hole should be kept even for the thicker screen case. This feature has been confirmed in the previous investigation [15]. By comparing Figure 5 with Figure 3, one finds little change in the upper scattering distribution (Figure 5(a)) but pretty big change in the lower scattering distribution (Figure 5(b)). This is due to the fact that the truncated incident GO beam experiences the reflection at the hole's internal wall to change the beam propagation direction in the lower half-space, as shown in Figure 5(c). From this result, one should be careful about the thickness of the hole, as it becomes thicker with respect to the wavelength.

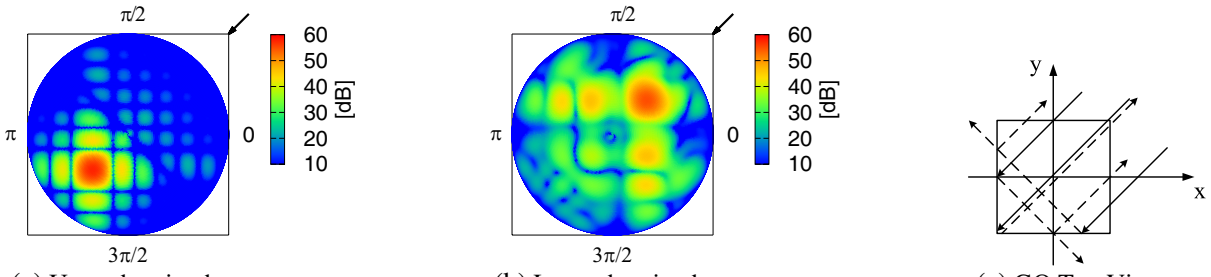

(a) Upper hemi-sphere (b) Lower hemi-sphere (c) GO Top View

Figure 5. TE scattering field strength map for $\theta_0 = \pi/6$, $\phi_0 = \pi/4$, $ka = kb = 30$, $kc = \sqrt{6}ka$. (a) Scattering field strength map on the upper hemisphere. (b) Scattering field strength map on the lower hemisphere. (c) Top view of GO beam reflection at the holes internal wall.

Let us now discuss the effect of the window glass with practical parameters for mobile communications. The frequency is set to be 1 GHz; the dimension of the window frame of the building wall is chosen as $a = 1.0\,\mathrm{m}$, $b = 2.2\,\mathrm{m}$, $c = 0.15\,\mathrm{m}$; and the window glass of the thickness $c_2 - c_1 = 0.008\,\mathrm{m}$ is installed on the upper aperture ($c_1 = 0$). The electric property of the glass is selected as $\varepsilon_r = 7.2 - j0.151$, $\mu_r = 1$ for soda-silica glass [19].

Figures 6, 7 show the scattering field distribution of co-polarized (E_ϕ) component for the TE polarized incidence, and Figures 8, 9 show the co-polarized (E_θ) component for the TM case. The main scattering feature is the same for both TE and TM cases, and the scattering field is distributed in the vicinity of the reflected and transmitted GO beam directions. In order to observe the effect of the window glass, the scattering patterns are shown in detail in the plane of the incidence ($\phi = \phi_0$, $\phi_0 + \pi$) and in the plane perpendicular to the incidence ($\phi = \phi_0 + \pi/2$, $\phi_0 + 3\pi/2$) in Figures 7, 9. As seen clearly from these figures, the scattering occurs mainly in the incident plane and the main scattering beam peaks become lower by $1 \sim 2\,\mathrm{dB}$. Since the glass is pretty thin ($c_2 - c_1 < 0.1\lambda$) and its loss is small, the effect is weak to the scattering far-field. Through the secondary radiation $\mathbf{E}^{\mathrm{s}}_{11}$, several minor lobes are generated by the glass layer especially in the upper half region.

TE polarized plane wave scattering far-field E_ϕ and TM polarized plane wave scattering far-field

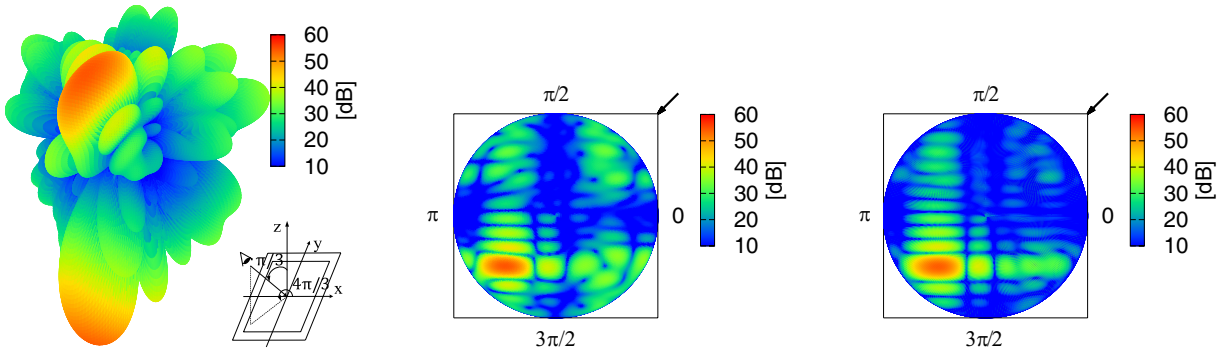

(a) E_ϕ (TE polarization) (b) Upper hemi-sphere (c) Lower hemi-sphere

Figure 6. TE scattering far-field patterns of E_ϕ component by a rectangular glass window. $\theta_0 = \pi/4$, $\phi_0 = \pi/4$. $a = 1.0\,\mathrm{m}$, $b = 2.2\,\mathrm{m}$, $c = 0.15\,\mathrm{m}$. The location of a dielectric glass ($\varepsilon_r = 7.2 - j0.151$, $\mu_r = 1$) is set at the upper aperture ($c_1 = 0\,\mathrm{m}$, $c_2 = 0.008\,\mathrm{m}$). Frequency $f = 1\,\mathrm{GHz}$. (a) Three-dimensional pattern viewing from $\theta = \pi/3$, $\phi = 4\pi/3$. (b) Scattering field strength map on the upper hemisphere. (c) Scattering field strength map on the lower hemisphere.

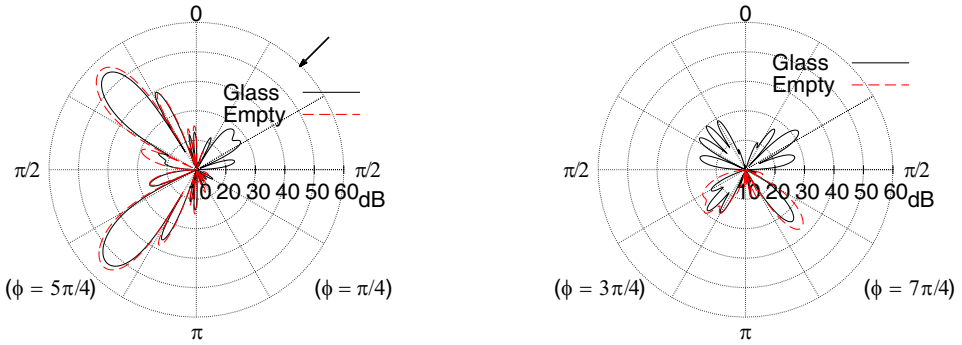

(a) Incident Plane ($\phi = \pi/4$, $5\pi/4$) (b) Plane ($\phi = 3\pi/4$, $7\pi/4$)

Figure 7. Comparison of TE polarized scattering far-fields $\mathbf{E}_\phi$ in θ variation with and without a window glass. $a = 1.0\,\mathrm{m}$, $b = 2.2\,\mathrm{m}$, $c = 0.15\,\mathrm{m}$, $\theta_0 = \pi/4$, $\phi_0 = \pi/4$. The location of a dielectric glass ($\varepsilon_r = 7.2 - j0.151$, $\mu_r = 1$) is set at the upper aperture ($c_1 = 0\,\mathrm{m}$, $c_2 = 0.008\,\mathrm{m}$). (a) Incident Plane ($\phi = \pi/4$, $5\pi/4$). (b) Plane perpendicular to the incident plane ($\phi = 3\pi/4$, $7\pi/4$).

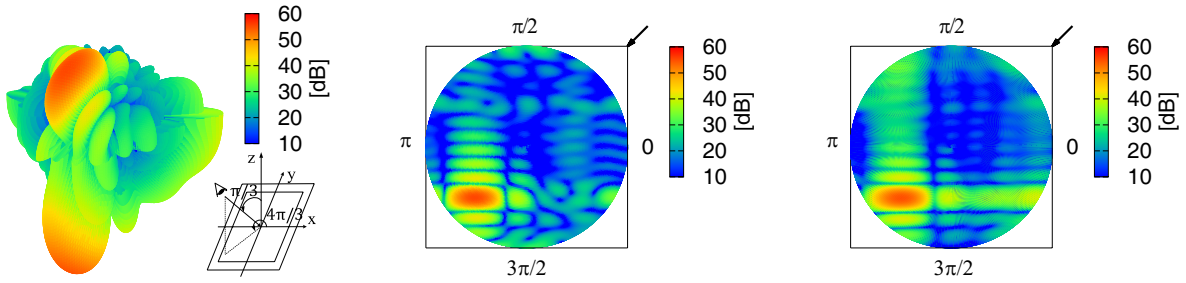

(a) E_ϕ (TM polarization) (b) Upper hemi-sphere (c) Lower hemi-sphere

Figure 8. TM scattering far-field patterns of E_θ component by a rectangular glass window. All parameters are the same as Figure 6. (a) Three-dimensional pattern viewing from $\theta = \pi/3$, $\phi = 4\pi/3$. (b) Scattering field strength map on the upper hemisphere. (c) Scattering field strength map on the lower hemisphere.

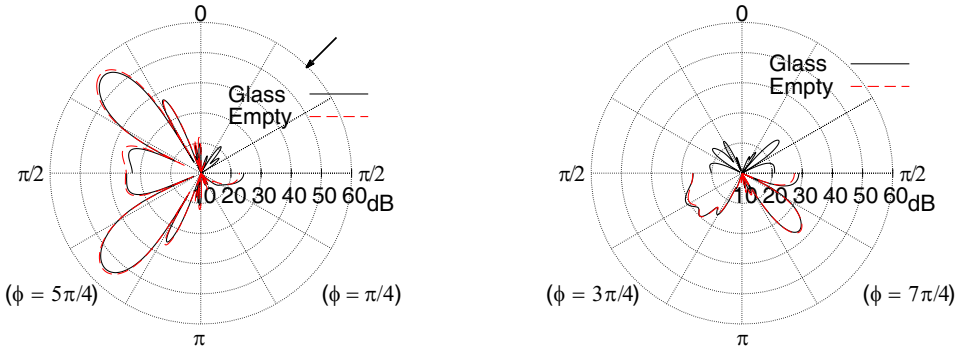

(a) Incident Plane ($\phi = \pi/4, 5\pi/4$) (b) Plane ($\phi = 3\pi/4, 7\pi/4$)

Figure 9. Comparison of TM polarized scattering far-fields E_θ in θ variation with and without a window glass. All parameters are the same as Figure 7. (a) Incident Plane ($\phi = \pi/4, 5\pi/4$). (b) Plane perpendicular to the incident plane ($\phi = 3\pi/4, 7\pi/4$).

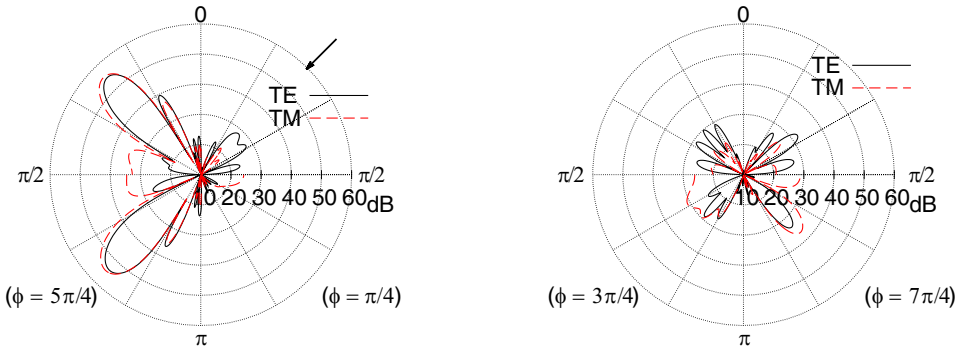

(a) Incident Plane ($\phi = \pi/4, 5\pi/4$) (b) Plane ($\phi = 3\pi/4, 7\pi/4$)

Figure 10. Comparison of TE polarized scattering far-fields E_ϕ and TM polarized scattering far-fields E_θ in θ variation by a rectangular glass window. All parameters are the same as in Figure 7. (a) Incident Plane ($\phi = \pi/4, 5\pi/4$). (b) Plane perpendicular to the incident plane ($\phi = 3\pi/4, 7\pi/4$).

E_θ are compared in Figure 10. While the intensities of the scattering fields at the main beam directions are almost the same, there are differences at side lobes and near the boundary direction. One might also see the difference near the boundary direction in the perpendicular plane. The difference at the boundary direction ($\theta = \pi/2$) is caused by the fact that E_ϕ of TE polarization vanishes due to the

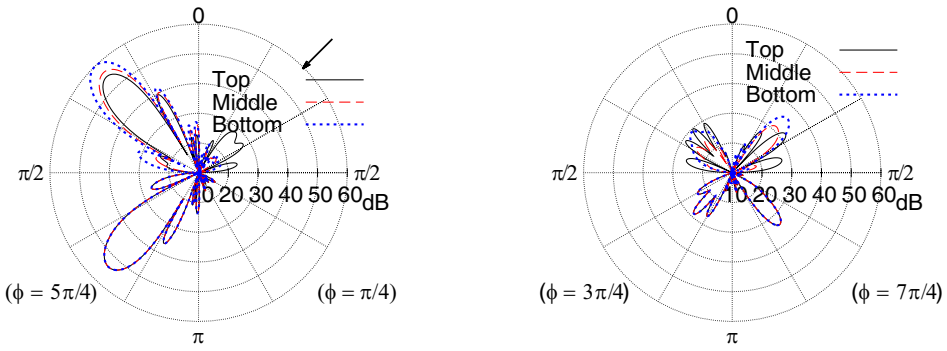

Figure 11. Comparison of TE polarized scattering far-fields E_ϕ in θ variation due to the location of the window glass. $a = 1.0\,\text{m}$, $b = 2.2\,\text{m}$, $c = 0.15\,\text{m}$, $\theta_0 = \pi/4$, $\phi_0 = \pi/4$. Position of a window glass ($\varepsilon_r = 7.2 - j0.151$, $\mu_r = 1$) is changed at the top, the middle, and the bottom. (a) Incident plane ($\phi = \phi_0$, $\pi + \phi_0$). (b) Plane perpendicular to the incident plane ($\phi = 3\pi/4$, $7\pi/4$).

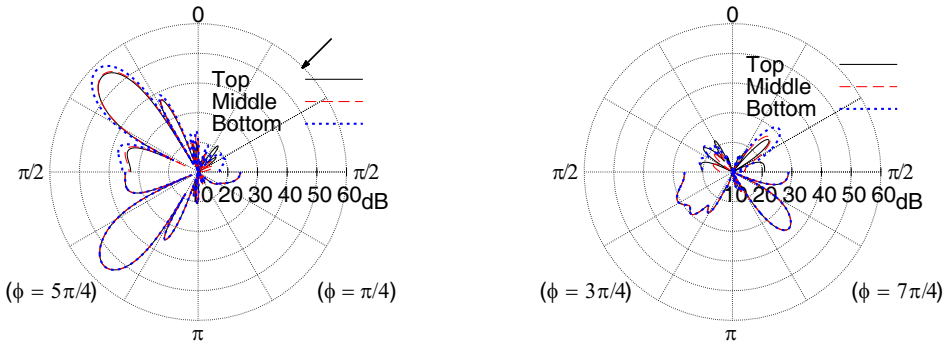

Figure 12. Comparison of TM polarized scattering far-field E_θ in θ variation due to the location of the window glass. All parameters are the same as in Figure 11. (a) Incident plane ($\phi = \phi_0$, $\pi + \phi_0$). (b) Plane perpendicular to the incident plane ($\phi = 3\pi/4$, $7\pi/4$).

pattern functions in Eqs. (9), (28), and (33), while E_θ in TM polarization remains. Also one finds a slight change of the main scattering lobe direction between TE and TM polarizations.

Figures 11, 12 show the co-polarization pattern change due to the location of the glass for TE and TM polarizations, respectively. The location of the glass is changed at the top ($c_1 = 0$), the middle ($c = c_1 + c_2$), and the bottom ($c_2 = c$). The location of the window glass creates a change of the scattering pattern in the upper region. When one compares the empty case in Figures 7, 9, the difference among the three cases at the main scattering beam peaks is approximately $2 \sim 3\,\text{dB}$. However, there is no change in the lower region since the modal fields which excite the transmitted field at the bottom aperture to the lower region are essentially the same no matter where the internal glass layer is located. These observations can be applied for both polarization cases.

It might be interesting to analyze the scattering far-field by a square aperture case ($a = b = 1.0\,\text{m}$). Figures 13, 14 show the comparison of the scattered far-fields by the square empty and the square glass windows with the glass set at the top aperture ($c_1 = 0$). Again the glass effect is small to the main lobes, but the scattering lobes become broader and small. This feature can be explained from the scattering pattern function A in Eq. (10), which is a product of two sinc functions. This pattern function A has a peak value of $k^2ab/4$ at the specular reflection direction and oscillates rapidly as the aperture becomes larger. When the scattering patterns in Figures 7, 9 are compared with those in Figures 13, 14, there are more sharp diffraction lobes constructed for the wide aperture due to the interference between the diffracted fields excited at the aperture's edges. The scattering far-fields in the plane perpendicular to

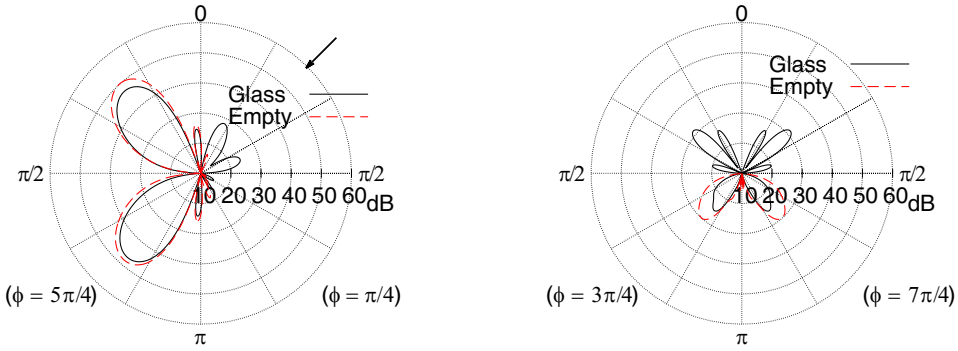

(a) Incident Plane ($\phi = \pi/4, 5\pi/4$) (b) Plane ($\phi = 3\pi/4, 7\pi/4$)

Figure 13. Comparison of TE polarized scattering far-fields $\boldsymbol{E}_\phi$ in θ variation with and without a window glass. All parameters are the same as in Figure 10 except $b = 1.0\,\text{m}$. (a) Incident Plane ($\phi = \pi/4, 5\pi/4$). (b) Plane perpendicular to the incident plane ($\phi = 3\pi/4, 7\pi/4$).

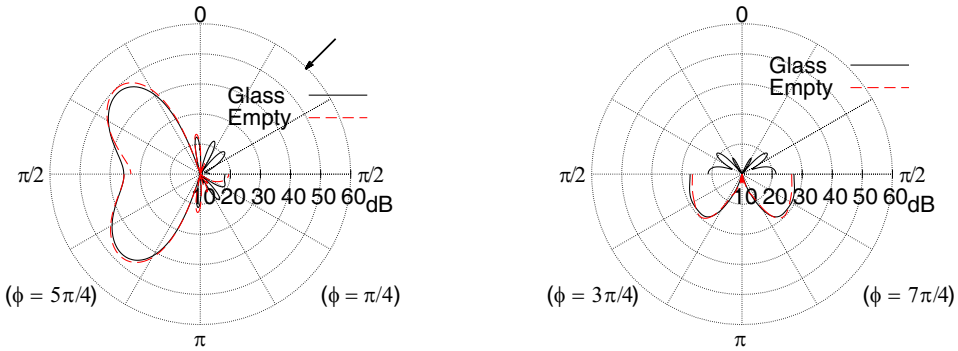

(a) Incident Plane ($\phi = \pi/4, 5\pi/4$) (b) Plane ($\phi = 3\pi/4, 7\pi/4$)

Figure 14. Comparison of TM polarized scattering far-fields $\mathbf{E}_\theta$ in θ variation with and without a window glass. All parameters are the same as in Figure 13. (a) Incident Plane ($\phi = \pi/4, 5\pi/4$). (b) Plane perpendicular to the incident plane ($\phi = 3\pi/4, 7\pi/4$).

the incident plane in Figures 13(b), 14(b) are found to be symmetric with respect to the z-axis due to the symmetry of the coefficient $B_{m,n}$ in Eq. (29) when $a = b$ and $\phi = (3\pi/4, 7\pi/4)$.

4. CONCLUSION

In this study, KA method has been utilized to formulate the scattering fields by a rectangular hole with a material slab layer to simulate the scattering from a window glass on a building wall. The scattering field can be obtained by the radiation from the equivalent magnetic currents excited successively on the virtually closed apertures of the hole. The penetrating field inside the hole has been expressed in terms of the waveguide modes, and these modal fields are used for estimating additional scattering fields in the upper and lower regions. The comparison of numerical results with the KP method has been made for the empty case [15] to check the accuracy of our formulations, and good agreement has been found between them. The effect of the window aperture dimension, slab layer, and polarization has also been discussed. The increasing thickness of the wall mainly impacts on the lower scattering far-field pattern. If one only concerns with the main beam of the scattered field, it can be roughly estimated by a somewhat simpler empty case.

Penetration through a practical lossy wall of the building, the effect of multiple windows, and the surface roughness of the wall are also important in practical applications for wireless communication environment. These aspects are now under investigation.

ACKNOWLEDGMENT

A part of this work is supported by the JSPS KAKENHI Grant Number 19K04398.

REFERENCES

1. Bertoni, L. H., *Radio Propagation for Modern Wireless Systems*, Prentice-Hall, New Jersey, 2000.
2. Morse, P. M. and P. J. Rubenstein, "The diffraction of waves by ribbons and by slits," *J. Appl. Phys.*, Vol. 54, No. 11, 895–898, Dec. 1938.
3. Kashyap, S. and M. A. K. Hamid, "Diffraction characteristics of a slit in a thick conducting screen," *IEEE Trans. Antennas and Propag.*, Vol. 19, No. 4, 499–507, Jul. 1971.
4. Kang, S. H., H. J. Eom, and T. J. Park, "TM scattering from a slit in a thick conducting screen: Revisited," *IEEE Trans. Microw. Theory Techn.*, Vol. 41, No. 5, 895–899, May 1993.
5. Park, T. J., S. H. Kang, and H. J. Eom, "TE scattering from a slit in a thick conducting screen: Revisited," *IEEE Trans. Antennas and Propag.*, Vol. 42, No. 1, 112–114, Jan. 1994.
6. Jin, J. M. and J. L. Volakis, "TE scattering by an inhomogeneously filled aperture in a thick conducting plane," *IEEE Trans. Antennas and Propag.*, Vol. 38, No. 8, 1280–1286, Aug. 1990.
7. Jin, J. M. and J. L. Volakis, "Electromagnetic scattering by and transmission through a three-dimensional slot in a thick conducting plane," *IEEE Trans. Antennas and Propag.*, Vol. 39, No. 4, 543–550, Apr. 1991.
8. Hongo, K. and G. Ishii, "Diffraction of an electromagnetic plane wave by a thick slit," *IEEE Trans. Antennas Propag.*, Vol. 26, No. 3, 494–499, May 1978.
9. Serizawa, H., "Diffraction by a rectangular hole in a thick conducting screen," Open access peer-reviewed chapter, IntechOpen, 2019.
10. Shirai, H., M. Shimizu, and R. Sato, "Hybrid ray-mode analysis of E-polarized plane wave diffraction by a thick slit," *IEEE Trans. Antennas and Propag.*, Vol. 64, No. 11, 4828–4835, Nov. 2016.
11. Shimizu, M., H. Shirai, and R. Sato, "Electromagnetic scattering analysis by a window model on a building wall," *IEICE Trans. on Electron.*, Vol. J100-C, No. 7, 295–301, Jul. 2017 (in Japanese).
12. Felsen, L. B. and H. Shirai, "Hybrid ray-mode analysis of high-frequency wave coupling into large waveguides and cavities," *Optics Lett.*, Vol. 12, No. 1, 7–9, 1987.
13. Shirai, H. and L. B. Felsen, "Rays, modes and beams for plane wave coupling into a wide open-ended parallel-plane waveguide," *Wave Motion*, Vol. 9, No. 4, 301–317, Jul. 1987.
14. Nguyen, K. N. and H. Shirai, "Kirchhoff approximation analysis of plane wave scattering by conducting thick slits," *IEICE Trans. on Electron.*, Vol. E102-C, No. 1, 12–20, Jan. 2019.
15. Nguyen, K. N., H. Shirai, and H. Serizawa, "Electromagnetic scattering analysis from a rectangular hole in a thick conducting screen," *IEICE Trans. on Electron.*, Vol. E104-C, No. 4, 134–143, 2021.
16. Balanis, C. A., *Advanced Engineering Electromagnetics*, 2nd Edition, Wiley, New Jersey, 2012.
17. Felsen, L. B. and N. Marcuvitz, *Radiation and Scattering of Waves*, Prentice-Hall, New Jersey, 1973.
18. Shirai, H., *Geometrical Theory of Diffraction*, Corona Publishing Co., Ltd., 2015 (in Japanese).
19. Von Hippel, A. R., *Dielectric Materials and Applications*, John Wiley & Sons, New York, 1954.